

# 9 new M Dwarf Planet Candidates from TESS Including 5 Gas Giants

Yoshi Nike Emilia Eschen,<sup>1,2</sup> Michelle Kunimoto,<sup>1</sup>★

<sup>1</sup>*Department of Physics and Kavli Institute for Astrophysics and Space Research, Massachusetts Institute of Technology,  
77 Massachusetts Avenue, Cambridge, MA 02139, USA*

<sup>2</sup>*Department of Physics, University of Warwick, Gibbet Hill Road, Coventry, CV4 7AL, UK*

Accepted XXX. Received YYY; in original form ZZZ

## ABSTRACT

We present the detection of 9 new planet candidates orbiting M dwarfs, identified using an independent search and vetting pipeline applied to TESS Full-Frame Image (FFI) data from Sectors 1 to 63. Our candidates include planets as small as  $1.4 R_{\oplus}$ , with orbital periods up to 20 days. Among the 9 new candidates, we identified 5 gas giants, which represent a rare and unexpected outcome of planet formation. Our findings add to the growing sample of giant planets around M dwarfs found by TESS. We discuss their follow-up potential for mass measurements through radial velocity observations and atmospheric characterization through transmission spectroscopy. We highlight TIC 12999193.01 as a particularly unique gas giant candidate in an eccentric orbit and excellent potential for atmospheric characterisation.

**Key words:** planets and satellites: detection – planets and satellites: gaseous planets – stars: low-mass – techniques: photometric – methods: data analysis

## 1 INTRODUCTION

The discovery of exoplanets has revolutionized our understanding of the prevalence, diversity, and formation of planetary systems. Among the myriad of exoplanetary hosts, M dwarfs have emerged as prime targets for exploration. These low-mass stars constitute the most abundant stellar population in the Milky Way, comprising around 70% of all stars (e.g., Henry et al. 2018). Due to being smaller and cooler, the habitable zones of M dwarfs (where liquid water could exist on a rocky planet’s surface) occur at much smaller orbital distances compared to Sun-like stars. Planets are also easier to detect around M dwarfs via the transit method due to the relatively large planet-to-star radius ratios, resulting in deeper transit depths.

Recognizing the unique advantages offered by M dwarfs, recent exoplanet research endeavors have increasingly focused on these low-mass stellar objects. In particular, NASA’s Transiting Exoplanet Survey Satellite (TESS; Ricker et al. 2015) has played a pivotal role by monitoring the brightness of stars across nearly the entire sky since its launch in 2018. Tens of thousands of M dwarfs have received at least one sector (27 days) of observations at a cadence of two minutes, as processed by NASA’s Science Processing Operations Center pipeline (SPOC; Jenkins et al. 2016), while millions more have data available at longer cadence (between 30 minutes and 200 seconds) through Full Frame Image (FFI) observations. TESS has detected ~ 450 M dwarf planet candidates, including two Earth-sized planets in the habitable zones of M dwarfs (TOI-700d and e; Gilbert et al. 2020). Furthermore, among the most surprising TESS M dwarf planet discoveries have been a growing sample of gas giant planets. These are an particularly intriguing and rare phenomena, being significantly less common than hot Jupiters around Sun-like stars (Gan

et al. 2023; Bryant et al. 2023). Planet formation models struggle to reproduce the formation of gas giants, around low-mass stars, especially in close-in orbits, due to lack of formation time and materials in their protoplanetary disks (Burn et al. 2021).

Thanks to its frequent and expedited public data releases, TESS is also a fantastic source of data for community-led searches to contribute new planets. Independent planet detection and vetting pipelines include the TESS Faint Star Search (Kunimoto et al. 2022), DIAMante (Montalto et al. 2020), the Convolutional Neural Networks search for Transiting Planet Candidates (Olmschenk et al. 2021), and NEMESIS (Feliz et al. 2021). NEMESIS was explicitly dedicated to searching for M dwarf planets with TESS, for which it focused on single-sector light curves of 33,054 M dwarfs from Sectors 1 – 5.

In this work, we describe a new independent search for planets around over 100,000 M dwarfs with TESS, based on multi-sector Full Frame-Image (FFI) observations across Sectors 1 – 63. We build off vetting tests designed for the Faint Star Search and add new tests to distinguish planets from false positives. We present 9 new planet candidates obtained from this pipeline and their analysis.

## 2 METHODS

### 2.1 Lightcurve Generation

We started with all 117,475 M dwarfs ( $R_* < 0.6 R_{\odot}$ ,  $M_* < 0.6 M_{\odot}$ ,  $2400 < T_{eff} < 3900 K$ ) brighter than  $T = 13.5$  mag in the TESS Input Catalog (TIC) Candidate Target List (CTL) v8.01 (Stassun et al. 2019). Of our initial M dwarfs, 107,303 had light curves from the Quick-Look Pipeline (QLP; Huang et al. 2020) between sectors 1 and 63. QLP produces light curves using an aperture photometry approach combined with difference imaging, and has extracted light

★ Juan Carlos Torres Fellow

curves for all stars brighter than  $T = 13.5$  mag since the start of the TESS mission. The QLP dataset is the largest single source of publicly available light curves from TESS Full Frame Images to date.

The lightcurves were merged into multisector lightcurves to use all available data. We removed data flagged as poor quality (data with non-zero quality flags), resulting in stars having 17% of data removed on average. We then detrended the light curves using the biweight algorithm implemented in *wotan* (Hippke et al. 2019), using a detrending width of 0.75 days. Given that M dwarf planet transits are typically a few hours or shorter, this window was chosen to minimize the impact of transit distortion caused by detrending while removing long-term astrophysical trends.

## 2.2 Planet Search

We searched each multi-sector light curve using the Box-Least Squares (BLS: Kovács et al. 2002) algorithm implemented in *cuvarbase* (Hoffman 2022), which uses GPUs to speed up time series analysis. *cuvarbase* also adopts a Keplerian assumption to further optimize transiting planet searches, where only transit durations near the duration expected for a central, circular orbit at a given period and host star density are searched. The minimum period searched was set to 0.5 days, which was chosen to avoid unphysical orbits and reduce false positive contamination from stellar variability and contact binary stars at very short periods. The maximum period searched was set to half of the length of the longest continuous stretch of data (without sector-long gaps) or 100 days, whichever was smaller. The median star in our sample was searched for periods up to 25 days. To identify possible transit events, we required at least three transits and a signal-to-noise ratio (Hartman & Bakos 2016) greater than 9. A total of 13,642 signals met these detection criteria.

## 2.3 Candidate Vetting

We based our vetting procedure on the automated vetting described by the TESS Faint Star Search (Kunimoto et al. 2022), which has discovered more than 3000 new TESS Objects of Interest (TOIs) to date. In summary, the Faint Star Search vetting procedure automatically identifies astrophysical false positives (eclipsing binaries and nearby eclipsing signals) and false alarms (systematics, noise, and stellar variability) by searching for sinusoidal variations, similar events at the same timescale and significance of the candidate, significant odd-even transit depth differences, secondary eclipses, and highly grazing/large eclipses. The vetting procedure also produces and analyzes difference images to identify off-target eclipsing signals (Bryson et al. 2013) using the *transit-diffImage* codebase.<sup>1</sup>

After applying these tests to the signals meeting our detection criteria, we were still left with 2,928 passing signals (Figure 1), the vast majority of which should not be transiting planets. However, the Faint Star vetting procedure was originally designed to run after the *Astronet-Triage* machine learning classifier used by QLP (Yu et al. 2019; Tey et al. 2023) had removed most false alarms, and thus it is currently unsuitable to be a stand-alone vetting pipeline. We added new steps to further automate this procedure, which were run on all 13,642 signals alongside the Faint Star tests:

- We fit a trapezoid model to each signal, in addition to the transit models already fit in the Faint Star process.

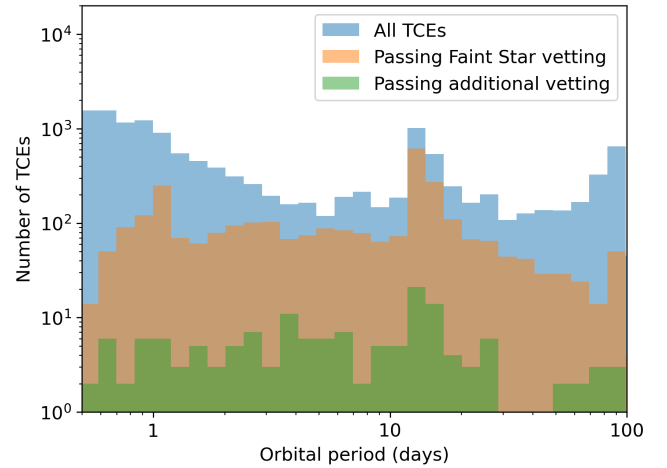


**Figure 1.** Period histogram of all TCEs passing basic detection criteria (blue). Roughly 20% of TCEs passed the Faint Star vetting procedure described by Kunimoto et al. (2022) (orange), which was designed to remove astrophysical false positives following false alarm rejection by *Astronet-Triage* (Tey et al. 2023). Only ~1% of all TCEs passed both the Faint Star vetting and our additional automated tests targeting false alarms (green). While we still see a systematic pileup near ~13.7 days (the TESS orbit), our final passing TCEs are more uniformly spread across orbital period. These TCEs were then assessed through manual vetting (§2.4).

- We added new tests to remove signals with unphysical orbits, which are likely false alarms due to stellar variability.
- We added a transit asymmetry test to identify false alarms that do not resemble symmetric, transit-like events.

These tests are described in more detail below.

### 2.3.1 Trapezoid Model Fit

The Faint Star procedure fits a transit model to each signal to derive important physical and orbital parameters, as well as to produce goodness-of-fit metrics to assess the consistency of the signal with a transit model. While we still adopted this step in the present work, we found that transit model fits would occasionally fail on signals that were clearly non-planet-like, had low signal-to-noise ratios, or were strongly affected by systematics. We found that trapezoid model fits were more robust to diverse signal shapes, providing us with useful metrics to further identify false positives.

The trapezoid model was parameterized by orbital period ( $P$ ), transit epoch ( $t_0$ ), transit depth ( $\delta$ ), the transit duration divided by the orbital period ( $q_{tran}$ ), and the transit ingress duration divided by the full transit duration ( $q_{in}$ ). A central, box-shaped transit should have a  $q_{in} \sim 0$ , while a grazing, V-shaped transit should have  $q_{in} \sim 0.5$ . To speed up the fit process, data more than two transit durations from the BLS-inferred center of each transit were ignored.

The results of the trapezoid model fit were used for new tests, as follows.

### 2.3.2 Unphysical Orbit Test

The transit model fit gives the ratio of the semi-major axis of the planet's orbit to the stellar radius,  $a/R_s$ . We removed 2,401 signals where the transit model fit returned  $a/R_s < 1.5$ , since these signals would likely result in planets within the Roche limit from their

<sup>1</sup> <https://github.com/stevepur/transit-diffImage>

stars and are hence in unphysical orbits. Although the minimum period searched by BLS should correspond to larger orbits for all stars in our sample, false positives can still return lower values through the transit model fit. Additionally, we found signals with durations significantly longer compared to our expectations for a circular orbit, which could indicate that the signal is caused by an eclipsing binary or stellar variability. We estimated the transit duration assuming a centrally transiting circular orbit and divided it by the orbital period to estimate  $q_{circ}$ , and compared this to the  $q_{tran}$  value obtained from the trapezoid model fit. We removed 7,760 signals with  $q_{circ}/q_{tran} < 0.5$ .

Finally, we flagged 141 signals with  $q_{tran} > 0.5$  as false positives, as this indicated that the signal occurred over half the orbital period, consistent with a contact binary system or stellar variability.

### 2.3.3 Transit Asymmetry Test

A common feature of other false alarms was asymmetry in the transits, which we identified by fitting half-trapezoid models to the left and right sides of the transits, separately. For these fits, we set the period, transit time, and depth equal to the original trapezoid fit results and let  $q_{tran}$  and  $q_{in}$  vary. We labeled a signal as a false alarm if the significance of the difference between the left and right  $q_{tran}$  values was  $> 5\sigma$ , rejecting 764 signals. Examples of symmetric and asymmetric events are shown in Figure 2.

## 2.4 Manual Triage

A total of 113 candidates survived the automated vetting procedure, 85 of which corresponded to known TOIs. Our pipeline did not flag any TOIs as false positives, with the exception of TOIs already dispositioned as false positives since being alerted.

We manually inspected the remaining 28 candidates by reviewing both flux and pixel-level diagnostics, and flagged another 17 signals as false positives. The majority of flagged signals were either borderline systematic or noise-like signals that were difficult for the vetter to distinguish from weak planet transit signals, or nearby eclipsing binaries (NEBs) in the same pixel as the target star which passed the automated check for centroid offsets. In summary, 9 non-TOI M dwarf planet candidates remained after visual inspection, with difference images indicating that the candidates are consistent with being co-located with their target stars (Figure 3).

## 2.5 Transit Model Fitting

We fit transit models with *exoplanet* (Foreman-Mackey et al. 2021) in order to obtain more accurate physical and orbital properties for the 9 new candidates. We used initial guesses obtained from the transit model fits used in automated vetting, and ran 4 chains with 2000 tuning steps and 2000 draw steps each. We confirmed that all chains converged according to the Gelman-Rubin convergence statistic for each parameter satisfying  $\hat{r} < 1.01$  (Gelman & Rubin 1992). The fitted properties are shown in Table 1, and final phase-folded light curves with the transit models overplotted are shown in Figure 4. The planet radius and semi-major axis for each candidate was derived using the transit model fit results and stellar properties provided in the TIC catalog (Table 2).

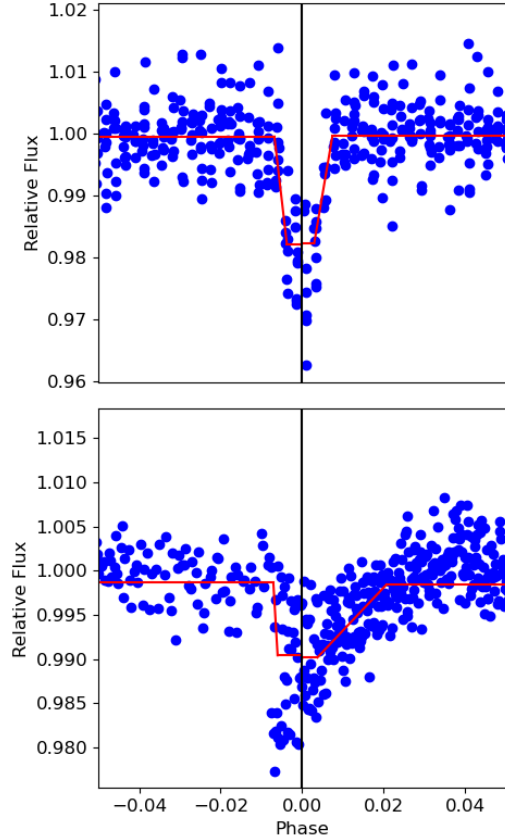


**Figure 2.** Top: An example of a symmetric transit, in this case the candidate around TIC 12999193. The red lines show half-trapezoid models separately fit to both left and right sides of the transit. Bottom: An example of an asymmetric signal caused by a systematic in the TESS data, with the associated half-trapezoid model fits.

## 2.6 False Positive Probabilities

To increase confidence in each candidate, we ran the TRICERATOPS statistical validation package (Giacalone & Dressing 2020; Giacalone et al. 2021) to estimate each planet's False Positive Probability (FPP) and Nearby False Positive Probability (NFPP). Since we lack follow-up data for our candidates, we use TRICERATOPS not to claim that any of our candidates are statistically validated, but to further support the interpretation that these are candidates suitable for further follow-up and eventual confirmation.

Because our multisector lightcurves covered the Prime, First, and Second Extended Mission, which had different exposure times, the phase curves inputted to TRICERATOPS were binned to a 30 minute cadence. Additionally, we only considered stars within 21 arcseconds as possible NEB sources given that our difference images were able to constrain the source of each signal to within a TESS pixel. We computed FPPs and NFPPs 20 times, and report the mean of these values to obtain a result more robust to outliers, shown in Table 3.

We omit FPP results for our three candidates with  $R > 8 R_{Earth}$ , as these are indistinguishable from brown dwarf and low-mass star scenarios based on TESS data alone, making their solutions degenerate and FPPs unreliable (Giacalone et al. 2021). All other candidates have low FPP ( $< 15\%$ ) and very low NFPP ( $< 1\%$ ), significantly improving confidence in their planet candidacy.

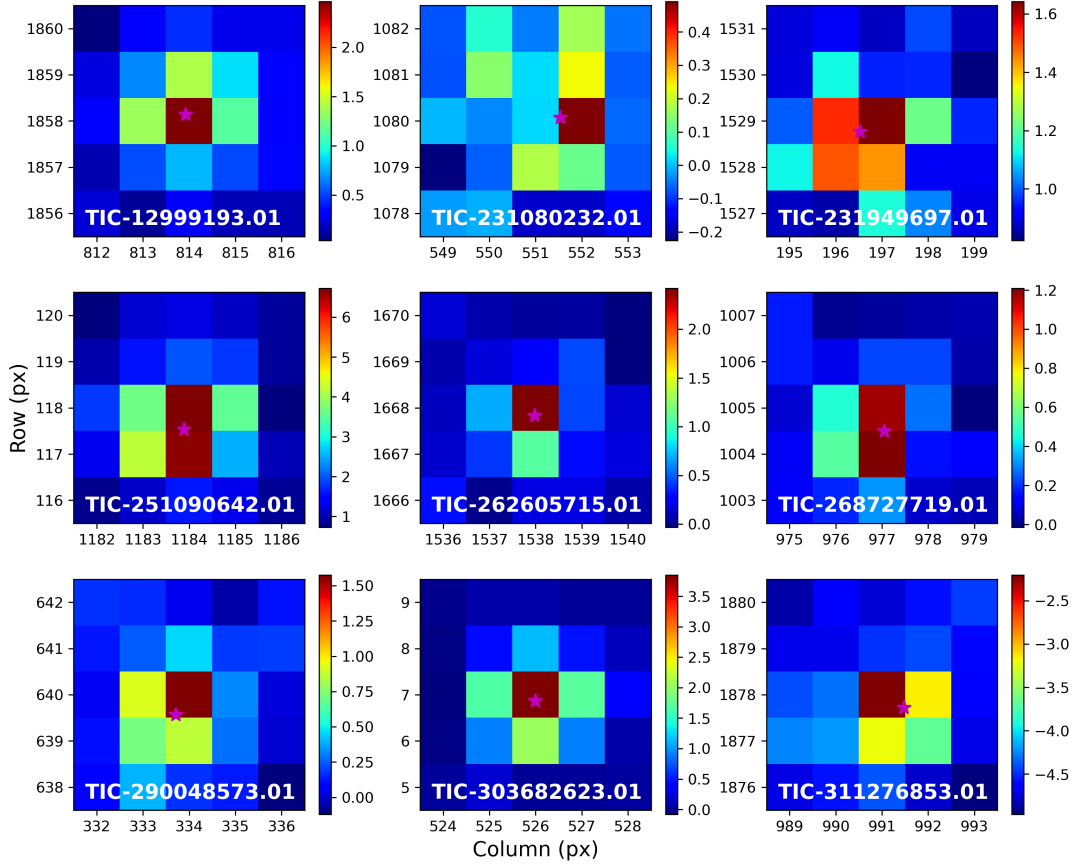


**Figure 3.** Difference images produced for each surviving candidate, made from the pixel time series of their most recently observed sectors. The pink star in each image indicates the location of the target star, showing that all passing candidates are consistent with on-target transiting planets.

TIC ID	Period (days)	Epoch (BJD)	$R_p/R_s$	Impact Parameter	Duration (hours)	Planet Radius ( $R_\oplus$ )	Semi-Major Axis (AU)
12999193	$1.482641^{+0.000002}_{-0.000002}$	$2458355.4444^{+0.0008}_{-0.0008}$	$0.357^{+0.139}_{-0.095}$	$1.146^{+0.159}_{-0.122}$	$0.63^{+0.33}_{-0.23}$	$9.78^{+3.83}_{-2.61}$	$0.0154^{+0.0005}_{-0.0005}$
231080232	$12.55434^{+0.00009}_{-0.00009}$	$2458336.848^{+0.006}_{-0.005}$	$0.037^{+0.002}_{-0.002}$	$0.314^{+0.112}_{-0.172}$	$2.80^{+0.14}_{-0.18}$	$2.23^{+0.15}_{-0.15}$	$0.086^{+0.001}_{-0.001}$
231949697	$0.907204^{+0.00003}_{-0.00004}$	$2458468.628^{+0.003}_{-0.003}$	$0.026^{+0.002}_{-0.002}$	$0.650^{+0.056}_{-0.103}$	$0.88^{+0.06}_{-0.10}$	$1.41^{+0.09}_{-0.11}$	$0.0145^{+0.0002}_{-0.0002}$
251090642	$20.04169^{+0.00004}_{-0.00004}$	$2458879.409^{+0.001}_{-0.001}$	$0.184^{+0.002}_{-0.002}$	$0.063^{+0.064}_{-0.045}$	$3.78^{+0.12}_{-0.12}$	$10.42^{+0.34}_{-0.33}$	$0.116^{+0.002}_{-0.002}$
262605715	$1.161258^{+0.00002}_{-0.00002}$	$2458517.845^{+0.0009}_{-0.0009}$	$0.107^{+0.006}_{-0.005}$	$0.819^{+0.031}_{-0.042}$	$1.01^{+0.06}_{-0.07}$	$6.85^{+0.461}_{-0.41}$	$0.0180^{+0.0002}_{-0.0002}$
268727719	$0.6256828^{+0.000004}_{-0.000004}$	$2458766.5552^{+0.0006}_{-0.0006}$	$0.112^{+0.007}_{-0.006}$	$0.825^{+0.051}_{-0.042}$	$0.84^{+0.05}_{-0.06}$	$7.27^{+0.30}_{-0.43}$	$0.0120^{+0.0001}_{-0.0001}$
290048573	$1.483396^{+0.00004}_{-0.00004}$	$2458326.656^{+0.001}_{-0.002}$	$0.078^{+0.005}_{-0.005}$	$0.767^{+0.045}_{-0.070}$	$0.77^{+0.06}_{-0.08}$	$2.86^{+0.21}_{-0.20}$	$0.0174^{+0.0004}_{-0.0004}$
303682623	$0.6806129^{+0.000003}_{-0.000003}$	$2458438.5192^{+0.0005}_{-0.0004}$	$0.153^{+0.008}_{-0.006}$	$0.693^{+0.044}_{-0.037}$	$1.03^{+0.05}_{-0.05}$	$9.43^{+0.54}_{-0.49}$	$0.0125^{+0.0002}_{-0.0002}$
311276853	$5.16951^{+0.00003}_{-0.00003}$	$2458987.476^{+0.005}_{-0.004}$	$0.106^{+0.005}_{-0.007}$	$0.435^{+0.109}_{-0.200}$	$1.76^{+0.06}_{-0.06}$	$4.71^{+0.29}_{-0.32}$	$0.0430^{+0.0007}_{-0.0007}$

**Table 1.** Fitted and derived parameters for the 9 candidates based on exoplanet-fitted transit models.

TIC ID	RA (deg)	Dec (deg)	Tmag	Teff (Kelvin)	logg ( $\log \text{cm s}^{-2}$ )	Mass ( $M_\odot$ )	Radius ( $R_\odot$ )
12999193	346.857	-28.354	$13.366 \pm 0.007$	$3478 \pm 157$	$4.985 \pm 0.013$	$0.222 \pm 0.020$	$0.251 \pm 0.008$
231080232	68.018	-68.883	$12.870 \pm 0.007$	$3812 \pm 157$	$4.695 \pm 0.010$	$0.544 \pm 0.020$	$0.549 \pm 0.016$
231949697	94.258	-43.366	$11.330 \pm 0.007$	$3701 \pm 157$	$4.744 \pm 0.008$	$0.491 \pm 0.020$	$0.493 \pm 0.015$
251090642	139.794	53.595	$13.091 \pm 0.007$	$3560 \pm 157$	$4.720 \pm 0.009$	$0.518 \pm 0.020$	$0.520 \pm 0.015$
262605715	132.45	0.207	$12.555 \pm 0.007$	$3618 \pm 157$	$4.662 \pm 0.011$	$0.577 \pm 0.020$	$0.587 \pm 0.018$
268727719	347.957	65.23	$13.389 \pm 0.008$	$3718 \pm 157$	$4.657 \pm 0.011$	$0.582 \pm 0.020$	$0.593 \pm 0.018$
290048573	319.189	-25.786	$12.680 \pm 0.007$	$3518 \pm 157$	$4.888 \pm 0.001$	$0.318 \pm 0.020$	$0.336 \pm 0.010$
303682623	75.769	14.356	$13.018 \pm 0.008$	$3469 \pm 157$	$4.681 \pm 0.010$	$0.558 \pm 0.020$	$0.565 \pm 0.017$
311276853	247.739	26.107	$13.240 \pm 0.007$	$3583 \pm 157$	$4.823 \pm 0.004$	$0.396 \pm 0.020$	$0.404 \pm 0.012$

**Table 2.** Stellar parameters obtained from the TESS Input Catalogue v8.01 (Stassun et al. 2019) for the host stars.



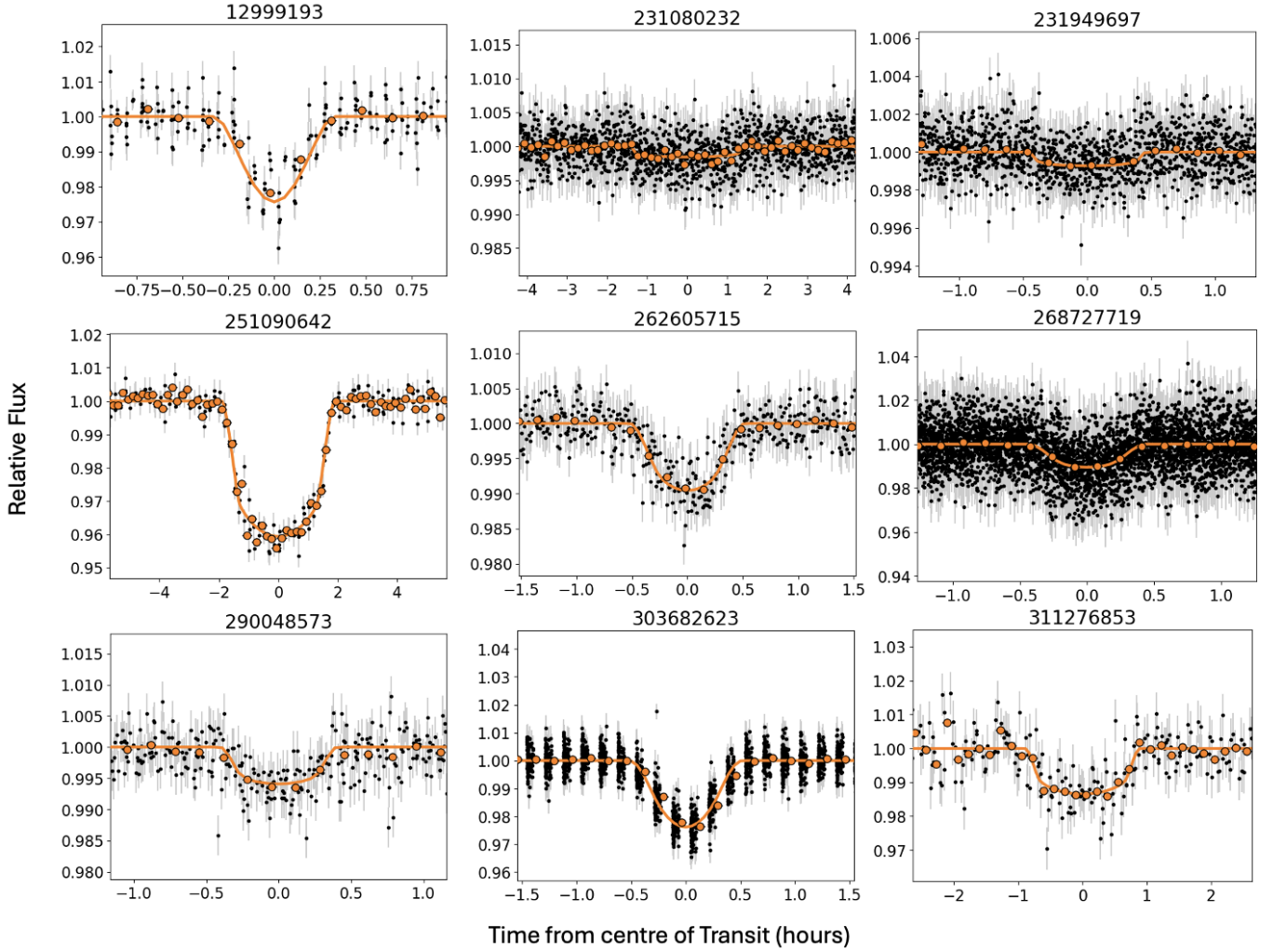


**Figure 4.** Phase curves for the 9 planet candidates, showing TESS data in black. Orange lines show fitted transit models, while orange circles represent the underlying data averaged every 15 minutes.

TIC ID	FPP	NFPP
12999193	-	0.0
231080232	0.031	0.0
231949697	0.122	0.002
251090642	-	0.0
262605715	0.0924	0.0
268727719	0.0364	0.0
290048573	0.030	0.006
303682623	-	0.0
311276853	0.036	0.0

**Table 3.** Triceratops Results for False Positive Probability (FPP) and Nearby False Positive Probability (NFPP) of each transit signal. FPPs are only provided for planets smaller than  $8R_{\oplus}$  due to degeneracies with brown dwarfs and low-mass stars.

### 3 RESULTS AND DISCUSSION

Our 9 planet candidates have sizes between 2 and 11 Earth radii and orbital periods between 0.6 and 20 days [Figure 5](#). All candidates orbit host stars fainter than  $T = 11$  mag, which is unsurprising given that brighter *M* dwarfs will have already been searched by the nominal QLP process ( $T < 10.5$  mag). All host stars are in the cool dwarf

catalogue ([Muirhead et al. 2018](#)), though follow-up spectroscopic observations would be valuable to better characterise the hosts and confirm their properties.

TIC 251090642.01, TIC 290048573.01 and TIC 303682623.01 are already known Community TESS Objects of Interest (CTOIs) listed on ExoFOP, and our derived parameters are within their reported errors. The other six candidates are new to this work.

#### 3.1 New Gas Giant Candidates

Five of our candidates may be gas giants based on their sizes ( $R_p > 6 R_{\oplus}$ ; TIC 12999193.01, TIC 251090642.01, TIC 262605715.01, TIC 268727719.01, TIC 303682623.01). Gas giants around *M* dwarfs are relatively scarce compared to those around Sun-like stars, potentially suggesting that their formation involves different mechanisms or conditions than those around larger stars ([Gan et al. 2023](#); [Bryant et al. 2023](#)). Current theories of planetary formation struggle to explain how gas giants could form in the relatively sparse protoplanetary disks that typically surround *M* dwarfs ([Dawson & Johnson 2018](#)). These disks contain less material compared to those around more

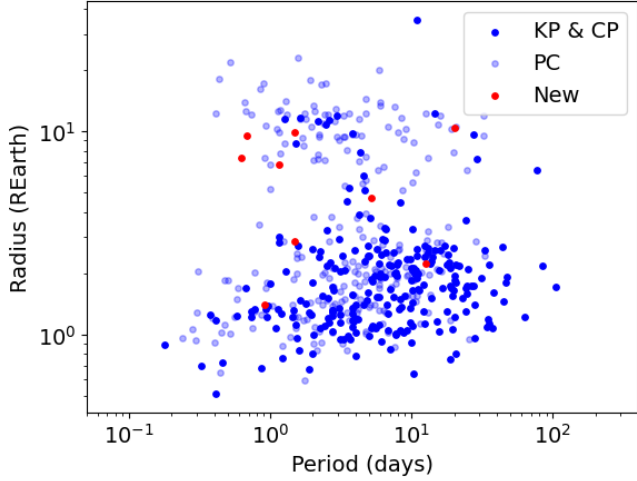


**Figure 5.** Distribution of planets and planet candidates around M dwarfs in radius-period space. Known and confirmed planets (KP & CP) were retrieved from the NASA Exoplanet Archive (NASA Exoplanet Archive 2024) (accessed on 2024 April 02) and plotted in blue, with planet candidates (PC) plotted in transparent blue. Our 9 candidates are plotted in red.

massive stars, making it challenging for gas giants to accrete enough mass (Burn et al. 2021).

Despite their rarity, TESS is finding a growing sample of giant planets around low-mass stars, especially hot Jupiters ( $R_p > 8 R_\oplus$  and  $P < 10$  days). To date, 11 M dwarf hot Jupiters have been confirmed, such as TOI-5205 b (Kanodia et al. 2023), HATS-71 (Bakos et al. 2020), and TOI-3235 (Hobson et al. 2023). If confirmed, our candidates would add another two hot Jupiters to this sample and provide new targets for further characterization. TIC-303682623.01 may also have the shortest orbital period of all known M dwarf gas giants to date, at  $P = 0.68$  days.

A major challenge with identifying gas giants around M dwarfs is that such objects are more likely to be eclipsing binary false positives compared to those around Sun-like stars. Based on Gaia DR3 observations (Gaia Collaboration et al. 2016, 2023), our giant candidate hosts TIC 12999193, 251090642, and 268727719 all have low Renormalized Unit Weight Error (RUWE) values (1.17, 1.09, 1.02) consistent with being single stars (Lindgren et al. 2018, 2021). TIC 303682623 was missing a RUWE value, and TIC 262605715 has evidence for binarity given  $\text{RUWE} = 2.81$  ( $> 1.4$ ); nevertheless, we retain it as a candidate in case it is a planet in a two-star system given we cannot reject a planet scenario at the level of the data, and we re-emphasize that follow-up of all of our candidates will be needed for confirmation and better characterisation of the host stars.

There are additional challenges associated with estimating accurate radii for objects grazing small hosts. Most of our giants have non-grazing impact parameters ( $b < 0.9$ ), suggesting that their planetary radius estimates are robust. However, the candidate orbiting the smallest star among our new hosts (TIC-12999193.01) has a highly grazing impact parameter ( $b = 1.1$ ), and its radius and duration estimates have large uncertainties, potentially further indicating an eccentric orbit. To explore the sensitivity of the transit model parameters to our assumption of circular orbits, we re-ran a further model fit using *exoplanet*, allowing eccentricity ( $e$ ) and argument of pericenter ( $\omega$ ) to vary. This fit converged at an eccentricity of  $0.469^{+0.111}_{-0.093}$  and planet radius of  $11.7^{+9.1}_{-5.4} R_\oplus$ . We compared the eccentric and circular models based on the leave-one-out cross-validation infor-

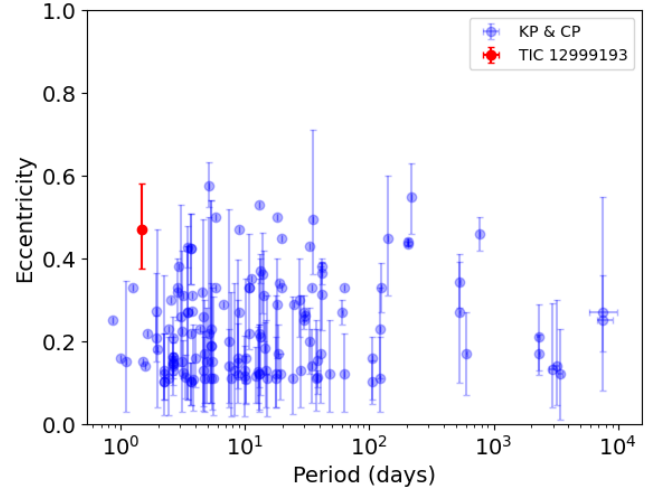


**Figure 6.** Eccentricities ( $> 0.1$ ) of known and confirmed planets (KP & CP) around M dwarfs obtained from the NASA Exoplanet Archive (NASA Exoplanet Archive 2024) (accessed on 2024 April 02) are plotted in blue. Our planet candidate is marked in red and has a period of 1.48 days.

mation criterion (LOO; Vehtari et al. 2015) as computed from the *exoplanet* results using the *arviz* package for analysis of Bayesian models (Kumar et al. 2019). LOO is a fully Bayesian model selection method that uses the entire posterior distribution. A model is favoured if it has a higher  $\log(\text{LOO})$  score. We found that the eccentric model was the preferred fit, with  $\Delta \log(\text{LOO}) = 9.38 \pm 3.64$  over the circular model. This eccentricity would be relatively high compared to other M dwarfs planets near its orbit (Figure 6). If TIC-12999193.01 is indeed a planet on an eccentric orbit, it will be an intriguing target for investigation into the high eccentricity migration scenario for M dwarf hot Jupiter origins.

Despite the relatively high likelihood that TIC-12999193.01 is a stellar object due to its grazing orbit, we opted to keep it as a possible planet to be added among other known highly grazing and eccentric hot Jupiters, such as HIP 65 A b (Nielsen et al. 2020) and Kepler-447 b (Lillo-Box et al. 2015). Follow-up radial velocity data could confirm (or deny) its planetary nature and provide a significantly more accurate estimate of its orbital eccentricity.

More generally, follow-up observations could provide key clues to differentiate between the different formation mechanisms explaining these rare planets, beyond the goal of their confirmation. Measurements of their orbital eccentricities with radial velocity data could suggest histories involving high-eccentricity migration, while characterisation of their atmospheres could suggest initial formation locations either close or far away from the host star. These planets will also be promising targets for investigations of star-planet interactions given their close-in orbits and much lower star-planet mass ratios compared to giants around Sun-like stars.

### 3.2 Follow-Up Potential

In order to check whether our candidates are suitable for radial-velocity (RV) follow-up, we calculate their semi-amplitude  $K$  using

$$K = 28.4 \left( \frac{M_P}{M_J} \right) \left( \frac{M_P + M_S}{M_\odot} \right)^{-1/2} \left( \frac{a}{1 \text{ AU}} \right)^{-1/2}, \quad (1)$$

TIC	Semi-Amplitude (m s <sup>-1</sup> )	TSM	ESM
12999193	106.348	700.703	209.067
231080232	2.327	18.140	0.636
231949697	2.744	8.644	6.682
251090642	28.274	105.508	5.927
262605715	33.293	162.580	60.509
268727719	44.926	150.005	71.931
290048573	10.311	128.535	15.854
303682623	70.038	264.880	151.459
311276853	13.772	83.136	8.259

**Table 4.** Computed semi-amplitude and Transmission and Emission Spectroscopy Metrics for each new planet candidate.

where  $K$  is in m s<sup>-1</sup> and the planet mass,  $M_p$ , is predicted via the mass-radius relations described by [Chen & Kipping \(2017\)](#). We also computed the Transmission and Emission Metric for each candidate ([Kempton et al. 2018](#)) to quantify their level of promise for atmospheric characterization through transmission and emission spectroscopy, respectively. The resulting RV semi-amplitudes, TSM, and ESM values are shown in Table 4.

Our best follow-up target is the gas giant candidate TIC 12999193.01, which features a large, easily-detectable RV semi-amplitude ( $K \sim 100$  m s<sup>-1</sup>) and one of the ten highest TSM values of all known M dwarf planets and planet candidates (TSM = 701). The ultra-short period gas giant candidate TIC-303682623.01 is also a promising follow-up target ( $K = 70$  m s<sup>-1</sup>, TSM = 265), especially given that its impact parameter is well-constrained and our estimate of its radius ( $R_p = 9.4 R_\oplus$ ) is more reliable. Among smaller planets ( $R < 4R_\oplus$ ), TIC-290048573.01 has  $K = 10.3$  m s<sup>-1</sup> and TSM = 129, sufficient to be considered an excellent target for characterization of sub-Neptunes according to thresholds described by [Kempton et al. \(2018\)](#).

#### 4 CONCLUSION

We present the detection of 9 planet candidates found in a multi-sector search of 107,303 M dwarfs with TESS data from Sectors 1 – 63. 3 of these candidates are already known CTOIs, while 6 are new to this work. Among our planet candidates, we find 5 gas giants, adding to a growing sample of gas giants around M dwarfs found by TESS which are challenging theories of planet formation and are intriguing targets for follow-up. One of these candidates (TIC 12999193.01) also potentially has a high eccentricity ( $e \sim 0.47$ ) and is hence an exciting target for further investigations into a possible origin through high-eccentricity migration. If confirmed, this candidate would be among the most eccentric short-period planets found around M dwarfs.

This work will be implemented into the Faint Star Search algorithm with further improvements to automate the entire vetting process, and to maximize planet yields from future community-led searches of TESS data.

#### ACKNOWLEDGEMENTS

We thank the referee for their feedback which improved the manuscript and clarified text. This paper includes data collected by the TESS mission, which are publicly available from the Mikulski Archive for Space Telescopes (MAST). Funding for the TESS mission is provided by NASA’s Science Mission directorate. We acknowledge the use of public TESS data from pipelines at the

TESS Science Office and at the TESS Science Processing Operations Center. This research has made use of the Exoplanet Followup Observation Program website, which is operated by the California Institute of Technology, under contract with the National Aeronautics and Space Administration under the Exoplanet Exploration Program. This research has made use of the NASA Exoplanet Archive, which is operated by the California Institute of Technology, under contract with the National Aeronautics and Space Administration under the Exoplanet Exploration Program. MK acknowledges support by the Juan Carlos Torres postdoctoral fellowship from the MIT Kavli Institute for Astrophysics and Space Research.

#### DATA AVAILABILITY

We make our fitted and derived planet parameters publicly available in a machine readable format. The lightcurves used for our search are already available as high-level science products (HLSPs) on MAST, from QLP.

#### REFERENCES

- Bakos G. Á., et al., 2020, *AJ*, **159**, 267  
 Bryant E. M., Bayliss D., Van Eylen V., 2023, *MNRAS*, **521**, 3663  
 Bryson S. T., et al., 2013, *Publications of the Astronomical Society of the Pacific*, **125**, 889  
 Burn R., Schlecker M., Mordasini C., Emsenhuber A., Alibert Y., Henning T., Klahr H., Benz W., 2021, *A&A*, **656**, A72  
 Chen J., Kipping D., 2017, *ApJ*, **834**, 17  
 Dawson R. I., Johnson J. A., 2018, *ARA&A*, **56**, 175  
 Feliz D. L., Plavchan P., Bianco S. N., Jimenez M., Collins K. I., Villarreal Alvarado B., Stassun K. G., 2021, *AJ*, **161**, 247  
 Foreman-Mackey D., et al., 2021, arXiv e-prints, p. arXiv:2105.01994  
 Gaia Collaboration et al., 2016, *A&A*, **595**, A1  
 Gaia Collaboration et al., 2023, *A&A*, **674**, A1  
 Gan T., et al., 2023, *AJ*, **165**, 17  
 Gelman A., Rubin D. B., 1992, *Statistical Science*, **7**, 457  
 Giacalone S., Dressing C. D., 2020, triceratops: Candidate exoplanet rating tool (ascl:2002.004)  
 Giacalone S., et al., 2021, *AJ*, **161**, 24  
 Gilbert E. A., et al., 2020, *AJ*, **160**, 116  
 Hartman J. D., Bakos G. Á., 2016, *Astronomy and Computing*, **17**, 1  
 Henry T. J., et al., 2018, *AJ*, **155**, 265  
 Hippke M., David T. J., Mulders G. D., Heller R., 2019, *AJ*, **158**, 143  
 Hobson M. J., et al., 2023, *ApJ*, **946**, L4  
 Hoffman J., 2022, cuvarbase: fast period finding utilities for GPUs, Astrophysics Source Code Library, record ascl:2210.030 (ascl:2210.030)  
 Huang C. X., et al., 2020, *Research Notes of the American Astronomical Society*, **4**, 204  
 Jenkins J. M., et al., 2016, in Chiozzi G., Guzman J. C., eds, Society of Photo-Optical Instrumentation Engineers (SPIE) Conference Series Vol. 9913, Software and Cyberinfrastructure for Astronomy IV. p. 99133E, doi:10.1117/12.2233418  
 Kanodia S., et al., 2023, *AJ*, **165**, 120  
 Kempton E. M. R., et al., 2018, *PASP*, **130**, 114401  
 Kovács G., Zucker S., Mazeh T., 2002, *A&A*, **391**, 369  
 Kumar R., Carroll C., Hartikainen A., Martin O., 2019, *Journal of Open Source Software*, **4**, 1143  
 Kunimoto M., et al., 2022, *The Astrophysical Journal Supplement Series*, **259**, 33  
 Lillo-Box J., Barrado D., Santos N. C., Mancini L., Figueira P., Ciceri S., Henning T., 2015, *A&A*, **577**, A105  
 Lindgren L., et al., 2018, *A&A*, **616**, A2  
 Lindgren L., et al., 2021, *A&A*, **649**, A2  
 Montalto M., et al., 2020, *MNRAS*, **498**, 1726

- Muirhead P. S., Dressing C. D., Mann A. W., Rojas-Ayala B., Lépine S., Paegert M., De Lee N., Oelkers R., 2018, *AJ*, **155**, 180
- NASA Exoplanet Archive 2024, Planetary Systems Composite Parameters, doi:10.26133/NEA13, <https://catcopy.ipac.caltech.edu/doi/doi.php?id=10.26133/NEA13>
- Nielsen L. D., et al., 2020, *A&A*, **639**, A76
- Olmschenk G., et al., 2021, *The Astronomical Journal*, **161**, 273
- Ricker G. R., et al., 2015, *Journal of Astronomical Telescopes, Instruments, and Systems*, **1**, 014003
- Stassun K. G., et al., 2019, *AJ*, **158**, 138
- Tey E., et al., 2023, *AJ*, **165**, 95
- Vehtari A., Gelman A., Gabry J., 2015, *arXiv e-prints*, p. arXiv:1507.04544
- Yu L., et al., 2019, *AJ*, **158**, 25

This paper has been typeset from a  $\mathrm{T}_{\mathrm{E}}\mathrm{X}/\mathrm{L}^{\mathrm{A}}\mathrm{T}_{\mathrm{E}}\mathrm{X}$  file prepared by the author.